15TH IEA HEAT PUMP CONFERENCE
MAY 26–29, 2026 | HOFBURG
VIENNA 2026
DECARBONISATION THROUGH INNOVATION

Energy optimization of a solar house using model predictive control for an integrated air-source heat pump water heater and radiant floor heating system

Yearim Yang[a,*], Andreas Athienitis[a]

a Centre for Zero Energy Building Studies, Concordia University, 1515 St.-Catherine St. West., Montreal, H3G 2W1, Canada

Abstract

This paper presents the application of a model predictive control strategy on an integrated thermal-energy system of a solar house with an air-source heat pump water heater (ASHPWH) connected to floor heating system, to minimize energy consumption while maintaining thermally acceptable indoor conditions in a cold climate. To prevent overheating and enhance overall energy efficiency, the integrated system utilizes preheated air from solarium as an air source for the ASHP and stores the heat for later use through a radiant floor heating system (RFHS). The cooled air from the ASHP evaporator is recirculated to another room for cooling, instead of exhausting it outdoors. A nonlinear model predictive control (NMPC) algorithm was developed for the nonlinear multi-objective optimization problem based on weather forecasts and predefined constraints during a limited prediction time horizon. A case study was conducted in two identical Test Cells at the Future Buildings Laboratory at Concordia University in Montreal, Canada, where one test cell simulated the solarium, where the indoor air temperature was permitted to exceed 28℃, and the other test cell was the climate-controlled zone. A low-order thermal network model was developed and calibrated using experimental data collected from March to May 2025. The energy performance of the NMPC was compared with two control strategies: rule-based control and a daytime charging control strategy. By coordinating the operation of the integrated energy system properly, NMPC reduced total daily energy consumption by 87.9% compared to the rule-based control strategy. Moreover, it maintained thermally comfortable conditions for 83.1% of the day on March 23rd, whereas rule-based control achieved 71.7% over the same period. Consequently, this research demonstrates that NMPC provides an effective control approach for the solar-driven ASHPWH-RFHS system, maintaining thermally acceptable indoor conditions and significantly enhancing energy efficiency in solar buildings.

Keywords: Noninear mdel predictive control; Air-source heat pump; Radiant floor heating system; Passive solar design

1. Introduction

In 2024, global electricity consumption increased by 1,100TWh, which is more than double the annual average growth over the past decade. Approximately 60% of this increase occurred in the building sector, fueled by rising demand for cooling, electrification, digitalization, and the rapid expansion of data centers. Fortunately, renewable energy and nuclear sources together provided 40% of global electricity generation. Although total energy-related carbon dioxide (CO_2) emissions still reached a record high of 37.8 Gt CO_2, it slowed down to 0.8% growth because of the expansion of solar and wind power, electric vehicles, and heat pumps. They reduced the annual fossil fuel energy demand by over 6% (30 EJ) and mitigated 2.6 billion tons of CO_2 emissions [1]. For the decarbonization of the building sector, the optimal integration of sustainable technologies in buildings has been increasingly investigated, with growing attention given to solar energy technologies and heat pumps.

A heat pump is an electrical device that extracts heat from a low-temperature source and transfers it to a higher-temperature sink. It offers stable heating and cooling performance and reduces primary energy consumption and carbon emissions compared to conventional gas boilers and electrical baseboard heaters. It

* Corresponding author. Tel.: +1-514-913-4857
E-mail address: ynaranghay11@gmail.com

may also facilitate demand-side flexibility if properly controlled [2]. Among them, air-source heat pump (ASHP) is the most widely adopted in buildings due to its affordability, operational stability, and ease of installation [3]. It utilizes air as the working source fluid to evaporate or condense the refrigerant passing through the heat exchanger coils. The performance of the ASHP is generally measured by using the coefficient of performance (COP), defined as the ratio of heat transfer rate released at the condenser to the work input to the compressor in heating mode. It can be expressed using the ideal Carnot efficiency for a heat pump operating between two temperature levels [4]. Its performance is highly dependent on the thermophysical properties of the refrigerant, heat exchanger design, and air-source temperature. Since ASHPs are often installed outdoors, efficiency diminishes sharply in the cold regions, increasing reliance on secondary heating systems [5].

By recognizing that the passive solar design spaces remain warmer than outdoors throughout the day, several studies have proposed ASHP configurations that draw preheated air from passive solar spaces. The elevated indoor temperatures result from the equator-facing large glazing units, which capture significant solar radiation, and from the thermal mass that gradually stores and releases the heat into the interior. However, in the absence of effective solar heat gain control, passive solar design spaces often experience daytime overheating, even in the heating season. Overheating causes occupant thermal discomfort but also increases energy consumption by encouraging uncontrolled window operation or auxiliary cooling system operation [6]. Coupling ASHPs with passive solar spaces mitigates these drawbacks on both sides: the ASHP gains efficiency from using a warmer and more stable air source, and its regulated heat extraction prevents the excessive heat buildup within the sunspaces, enhancing overall building energy performance. Touchie et al. [7] evaluated the energy performance of the retrofitted balcony sunspace with an ASHP in multi-unit residential buildings in Toronto, Canada, and determined that it can achieve 39% reduction in annual energy intensity and a 45% reduction in associated greenhouse gas emissions, compared to the baseline with baseboard heating. Sun et al. [3] utilized a dual-source heat pump to effectively extract the heated air from six Chinese-style greenhouses and transfer it to multi-span greenhouses. Their system achieved a COP between 4.3 and 4.8, while the COP of the ASHP using ambient air was between 3.4 and 3.5. Gaucher-Loksts et al. [8] compared the ASHP performance using three air sources: 1. Ambient air, 2. Preheated air from a building-integrated photovoltaic/thermal (BIPV/T) system, and 3. Preheated air from the solarium, under three different demand response strategies. The results presented that using preheated air from a solarium significantly improved the COP of the ASHP and achieved up to 80% energy saving in heating. Previous research applied conventional rule-based and demand response strategies to control the auxiliary system individually. But these methods cannot handle systems' complex nonlinear dynamics nor account for slow-response thermal inertia and fast-reacting auxiliary systems, resulting in suboptimal control and setpoint overshoot [9].

In recent years, improvements in building energy system operations have been proven to achieve as much as 30% of energy savings [10]. Model predictive control (MPC) is one of the promising advanced control strategies for optimizing building auxiliary systems. MPC determines the optimal control solutions by minimizing the multi-objective functions based on the weather forecast and constraints during a limited prediction time horizon, typically one day ahead [2]. MPC generates a sequence of future control actions during the control horizon, but only the first control action is applied at each timestep. The predicted system output is compared with the past measured data, and the optimization is repeated with the updated information[11]. MPC has been demonstrated to be effective in building energy management systems, achieving 26 to 40% energy savings by controlling the thermal mass energy storage capacity effectively [12]. Rastegarpour et al. [13] evaluated three MPC strategies to control an air-to-water heat pump coupled with a radiant floor heating system (RFHS). Their results presented that nonlinear MPC (NMPC) achieved 6% energy saving and improved thermal comfort by 4%. In contrast, linear time-varying MPC offered similar performance if a reference trajectory was provided, and the linear MPC was determined to be insufficient to address the nonlinear optimization problem effectively.

The optimization study of controlling solar-assisted air source heat pump water heater and RFHS system is underexplored, because of its unique energy configuration and complex nonlinearity. To improve their operation performance, this study evaluates the performance of an MPC-controlled ASHPWH-RFHS system in a research solar building, located in Montreal, Canada. The integrated energy system is designed to offset the limitations of individual components and enhance overall building energy efficiency, while maintaining thermally comfortable conditions. The ASHPWH is configured to use preheated air from the solarium and recirculate the cooled air from the ASHP evaporator outlet for cooling the heated room. The stored heat is later used for RFHS heating. NMPC is employed to optimize the control actions by simulating the building's indoor response to predicted weather forecasts within a prediction horizon and constraints. This study introduces a building energy model and a discretized water heater model to capture the temperature dynamics. System performance is compared across three control strategies: rule-based control, daytime charging control strategy, and NMPC. Results provide experimental data, identify the effectiveness and barriers of each control strategy, and offer a foundation for future research on the control of coupled solar driven energy systems.

2. Methods/Approach

By building upon the research by Gaucher-Loksts et al. [8], a case study was conducted at the Future Building Laboratory (FBL) at Concordia University in Montreal, Canada. The facility consists of five identical south-facing test cells, featuring an airtight envelope design and semi-transparent photovoltaic windows. Each cell measures 3.4m (W) x 3.05m (L) x 2.86m (H). For the experiment, Test Cells 3 functioned as a solarium where air temperature was permitted to exceed 28℃ and ranged from 18.9℃ to 36.3℃. Test Cell 4 served as the climate-controlled zone to which heat was delivered through the RFHS. Test Cell 3 is equipped with a fan coil unit, double-glazed low-e argon windows, and a 7.62 cm thick RFHS, while Test Cell 4 has venetian blind systems and a 10.16 cm thick RFHS. Test Cell 4 also includes double-glazed units in the middle section of the window, and triple- and quadruple- glazing units on the left and right sections of the windows, respectively. Their walls and ceiling are constructed with wood frames, gypsum boards, and insulation [14]. To balance the air pressure between two rooms, both test cells passively exchanged air through a small grille near the window, as shown in Fig.1. In the building energy model for rule-based control strategies, this was estimated at constant 0.5 ACH. For ease of computation in MPC, the thermal resistances and capacitances values are fixed constant; this inter-cell heat transfer rate was represented using a calibrated thermal resistance of 0.0145 ℃/W.

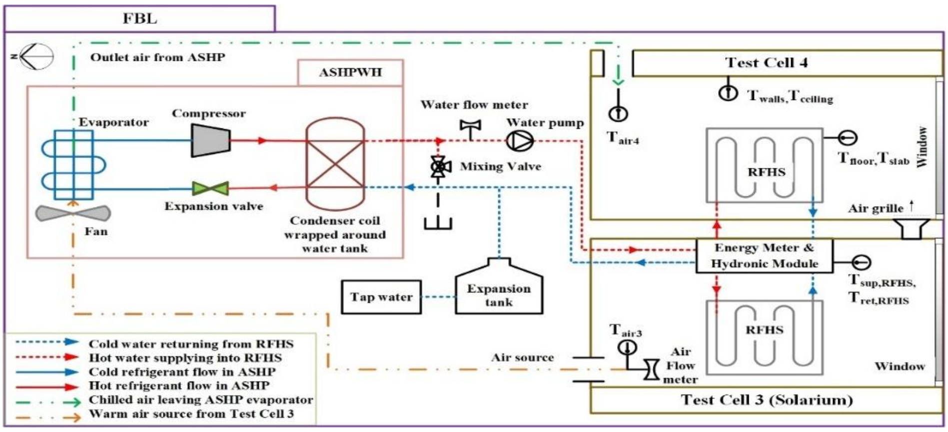

Figure 1. schematic of air, water, refrigerant cycles in ASHPWH-RFHS system in Test Cell 3 (solarium) and 4 (controlled zone).

When the ASPH operates, the warm air from Test Cell 3 is extracted through a ceiling inlet, using a fan attached to the ASHPWH. The air passes through the evaporator coil, transferring the heat to the refrigerant (R134a), and exits as cooled air at approximately 10℃ to 14.4℃. Instead of exhausting outdoors, this cooled air is supplied into Test Cell 4 via a ceiling outlet. The air mass flow rate was 0.04 kg/s, measured using an ALNor balometer. Notably, the actual fan speed may be slightly higher due to friction losses. The air inlet and outlet temperatures are measured at the center of Test Cell 3 and at the outlet of the ASHP evaporator, respectively. A closed-loop experiment without occupancy was conducted by closing the outlet of the main air handling unit and exhaust ventilation grilles on the ceiling to reduce uncertainties associated with air exchange with the other parts of the FBL. Thermostats were installed in each test cell and the mechanical room to measure the temperatures of the air, interior envelope surfaces, and concrete slab inside at 6 different heights and locations [14]. The energy meter in Test Cell 3 recorded the supply and return water temperatures and water mass flow rate at the RFHS. Meteorological data, including ambient temperature and global horizontal solar radiation were collected using a Lufft WS800-UMB weather station, installed on the roof of the FBL.

2.1. Mechanical systems

ProTerra hybrid electric ASHPWH was installed in the FBL mechanical room for easier duct integration between the rooms. The unit consists of a compressor, evaporator, fan, expansion valve, and a condenser coil wrapped around the exterior surface of the water tank, along with two electric resistance heating elements. The water heater has a rated water capacity of 170L. The allowed temperature range of the air source is from 2.8℃ and 62.7℃. The ASHPWH controller allows users to define water temperature setpoints and operation mode four times per day [15]. The unit operates in five modes: *Heat Pump, Electric, Energy Saver, High Demand, and Vacation*. For this experiment, only the *Heat Pump* and *Electric* modes were used. The ASHP has a rated input power of 1.2 kW at the compressor and a Uniform Energy Factor (UEF) of 3.75 [15]. UEF is the ratio of useful energy delivered to the water to energy used [16], which is often used as the energy performance metric for heat pump water heaters. In contrast, COP quantified HP performance by expressing the ratio of the heat output to the work input required to achieve that heat-transfer effect [4]. Due to the lack of detailed refrigerant-cycle and operational data for the ASHP, system performance was represented using an empirical correlation between COP and air-source temperature (T_{air3}) based on ASHPWH measurements (Eq. (1)) [17], incorporating the time interval, p. The heat transfer rate at the evaporator, Q_{evap}, was calculated using the measured air temperature in Test Cell 3 (inlet) and the outlet of ASHP (Eq. (2)). On the other hand, the *Electric* mode relies solely on the resistance heating elements, rated at 4.5 kW (upper) and 2.25 kW (lower). The COP of resistance elements was assumed to be 1.0.

$$COP_p = 0.00162 * T_{air3,p}^2 + 0.045 * T_{air3,p} + 1.038 \tag{1}$$

$$Q_{evap,p} = \dot{m}_{as} c_{p,as} (T_{air3,p} - T_{outlet,p}) \tag{2}$$

RFHS system was constructed using lightweight concrete with a thermal conductivity of 0.872 W/m°C and equipped with 107m of 1.59 cm-diameter PEX hydronic pipes. Pipes were arranged in a serpentine pattern on top of the floor insulation. The pipe spacing was 15.24 cm for the first three rows near the window and 22.86 cm for the remaining rows. The 8.9 cm of insulation has a thermal resistance of 1.77 m^2°C/W. The RFHS was controlled by a Tekmar zone valve controller, a microprocessor-based control module. The setpoint temperature of indoor air was set at 24°C between 7 AM and 7 PM and 20°C during the rest of the hours in all simulated control strategies. When a thermostat calls for heating, the zone valve opens, allowing the system to pump stored water at a constant rate of 0.0798 kg/s from the ASHPWH [14]. The heat transfer rate of the RFHS was estimated using the analytical equations proposed by Rastegarpour et al [13] (Eq. (3-4)).

$$T_{return,p} = (1 - exp(-\alpha))T_{slab,p} + exp(-\alpha)\, T_{w,top,p} \tag{3}$$

$$\alpha = \frac{U_{pipe}}{\dot{m}_w * c_{p,w}} \tag{4}$$

2.2. Building energy modeling

To track the dynamics of indoor temperatures and calculate the daily energy consumption, a resistance and capacitance (RC) modeling method was generated. In the RC model, temperature nodes, representing lumped control volumes of the building zone or envelopes, are interconnected through thermal resistances. The thermal resistance, *R*, represents the rate of conduction, convection, and radiation heat transfer, while the thermal capacitance, *C*, represents the amount of heat that needs to be absorbed or released to produce a unit temperature change at a node. For Test Cell 4, a 2 capacitance and 8 resistance (2C8R) model were generated by discretizing the zone into four temperature nodes, as shown in Fig. 2. The energy balance equations are discretized in time, p, and solved using an explicit finite difference method, as shown in Eq. (5), and rearranged to Eq. (6), corresponding to node, i [18]. The explicit finite difference method has the benefit of not needing to solve equations in every time step because the current time step temperature state is only influenced by the temperatures and heat sources at the previous time step [18]. The timestep was set to 3 minutes due to the comparably small size of the water heater compared to the zone thermal capacitances, calculated using Eq. (7). j represents all nodes connected to node i, and Q denotes a heat source such as radiant floor heating (*rfhs*), solar heat gains (*solargain*), or cooling.

$$C_i \frac{dT_i}{dt} = Q_i + \sum_{ij} \frac{T_i - T_j}{R_{i,j}} \tag{5}$$

$$T_{i,p+1} = \left(\frac{\Delta t}{C_i}\right)(Q_{solargain,p} + Q_{rfhs,p} + Q_{cooling,p} + \textstyle\sum_j (\frac{T_{j,p} - T_{i,p}}{R_{i,j}})) + T_{i,p} \tag{6}$$

$$\Delta t_{critical} = min\left(\frac{C_i}{\sum_j \frac{1}{R_{i,j}}}\right) \textit{for all nodes} \tag{7}$$

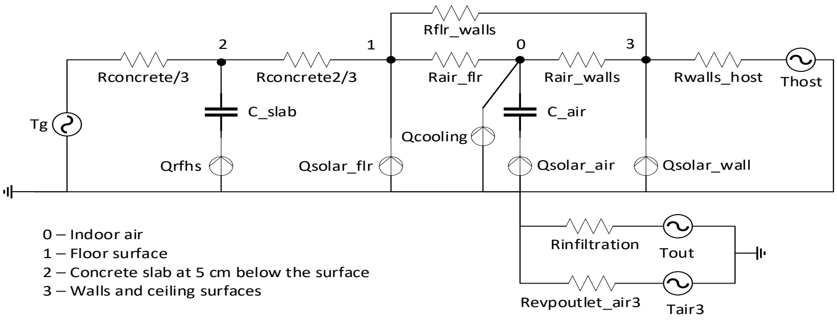

Figure 2. 2C8R thermal network of Test Cell 4.

In the 2C8R thermal network model, the state variables include the temperatures of indoor air, floor surface, concrete slab at 5cm below the surface (representing the midpoint of the concrete control volume), and the interior walls and ceiling surfaces, as shown in Fig. 2. In this study, thermal capacitances are assigned to the concrete floor (node 2) and indoor air (node 0). On the other hand, because the interior walls and ceiling have low thermal capacitance and have no direct interaction with the auxiliary system, their thermal capacitance is neglected. The heat sources interacting with these state variables comprise the outdoor air temperature, the main building temperature (adjacent zones that are not part of the experiment), the ground surface temperature, and the temperature of Test Cell 3. The ground surface temperature was set to constant 6°C. The main building temperature was measured in the mechanical room, as the door was always kept open, maintaining an air temperature comparable to the rest of the building (except the two test cells). Test Cell 3 air temperature was measured at the center of the room. The solar radiation incident on the interior surfaces was calculated by using Hottel's model [18] and assumed to be distributed on the floor surface (node 1) for 70%, on the walls and ceiling surface (node 4) for 30%, and on interior furniture attached to the air node (node 0) for 1%. The convective cooling heat transfer rate was computed using the constant air flow rate and air temperature difference at the inlet and outlet of the evaporator (Eq. (8)) and applied to air node 0. Air leakage and pressure drop effects in the duct systems were excluded due to the proximity between the mechanical room and Test Cell 4. Lastly, the radiative heating heat transfer rate was calculated using the return water temperature from RFHS and supply water temperature, as shown in Eq. (9), and applied at node 2.

$$Q_{cooling,p} = \dot{m}_a c_{p,a}\left(T_{outlet,p} - T_{0,p}\right) \tag{8}$$

$$Q_{rfhs,p} = \dot{m}_w c_{p,w}(T_{w,top,p} - T_{return,p}) \tag{9}$$

The water heater was modeled in a vertically discretized three-node model based on Rastegarpour et al.[13], as shown in Fig. 3. The three nodes of the model are indexed using i in the Eq. (10-12). The condenser heat transfer rate, $Q_{cond,i}$, was applied to the middle node, and the heat transfer from the tank wall to the room air, $Q_{host,i}$, occurred at all nodes. The top node had the outlet of water for the RFHS, and the return inlet was located at the bottom node. Additionally, the heat exchange between each node was presented in terms of $\dot{Q}_{i+1}$ and $\dot{Q}_{i-1.}$ The tank was assumed to be always full and had an equal mass flow rate at the outlet and inlet of the tank. In reference and daytime charging control strategies, the water mass flow rate was set at a constant of 0.0789 kg/s when RFHS was activated, which corresponds to the lowest speed setting of the three-speed wet-rotor circulator. In addition, the constant 0.02 kg/s mass flow rate was set inside the tank to represent the inversion mixing of the water and reduce the stratification based on Gaucher-Loksts et al. [8].

$$m_i c_p \frac{dT_i}{dt} = \dot{Q}_{cond,i} + \dot{Q}_{elec,i} - \dot{Q}_{host,i} + \dot{Q}_{i+1} - \dot{Q}_{i-1} + \dot{Q}_{conv,i} \tag{10}$$

$$\dot{Q}_{i+1} = (T_{i+1} - T_i)/R_{i,i+1} \;\; and \;\; \dot{Q}_{i-1} = (T_i - T_{i-1})/R_{i,i-1} \tag{11}$$

$$\dot{Q}_{conv,i} = \dot{m}_w c_{p,w}(T_{i+1} - T_i) \tag{12}$$

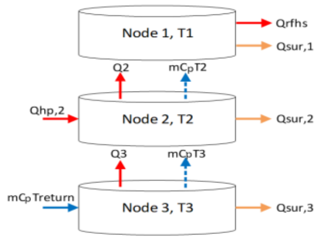

Figure 3. Schematic of heat transfers within the discretized water heater.

2.3. Validation and calibration

Initial calibration was performed using the conventional calibration and nonlinear least-squares fitting methods with measured indoor air temperature at Test Cells 3 and 4. These identified R and C parameter combinations that yield locally minimized errors were used as the initial estimates for the Bayesian calibration, which was carried out using the LMFIT [19]. Bayesian calibration is an iterative process of updating uncertainty distributions on the input parameters in a way that is consistent with the measured data. This method does not determine the one optimal value for each parameter but determines if this value for each parameter can provide a distribution of predicted outputs that are well aligned with the distribution of the observed data [20]. Since the objective of this research was to utilize surplus solar heat gain for nighttime heating via the ASHPWH, a calibration was conducted using cold and clear days' measurements. It is important to note that this solar-driven ASHP-TES mechanism is not intended for cloudy day conditions. Although several continuous clear days were available during the experiment, the selected four-days period (April 6th to April 9th) exhibited both strong solar gains and a wide ambient temperature fluctuation between -10℃ to 5℃. The normalized mean bias error (NMBE) and Coefficient of variation of root mean squared error (CV(RMSE)) are presented in Table 1. They were both within the ASHRAE Guideline 14 requirement of CV(RMSE) < 30% and NMBE < +/-10% [21]. Additionally, the water heater model was not calibrated due to insufficient manufacturer data and the inability to measure internal water temperature.

Table 1. Calibration result of RC thermal network using 4 days experimental data.

Calibration Method	NMBE	CV(RMSE)
Nonlinear least squares fitting	-0.33 %	5.98 %
Bayesian	-0.19%	4.19%

2.4. Control strategies

This paper compares the energy consumption and indoor thermal dynamics in Test Cell 4 on cold, clear days from March 21 to 23rd, 2025, under three control strategies: 1. Rule-based control (reference), 2. Daytime charging control, and 3. MPC. In reference, the water temperature setpoint is maintained at a constant 55℃, whereas daytime charging control strategy has charging and discharging periods. The water temperature setpoint increases to 55℃ during the charging period (12 PM-7 PM) and reduces to 43℃ during discharging period (7 PM-12 PM). Both control strategies originally operated the ASHP in *Heat Pump* mode throughout the day. However, simultaneous operations of the ASHP and RHFS occurred in the morning as both indoor air and water temperature dropped below their setpoints. Although the RFHS was often activated around 7 AM, the indoor air temperature did not increase quickly enough, and the stored warm water was depleted. Therefore, the ASHP was triggered to reheat the water while simultaneously supplying chilled outlet air to Test Cell 4. This undesirable condition continued because the convective cooling from ASHP reduced the indoor air temperature faster than the RFHS could raise it. To avoid this conflicting operation, both control strategies used *Electric* mode from 7 Am to 12 PM and *Heat Pump* mode for the remaining hours. Notably, the electric elements were operated when the mean water temperature drops below the minimum water temperature, 40℃. When the mean water temperature falls below 35℃, both elements are activated. When it is between 35℃ and 50℃, only the lower element operates, and when it is between 50℃ and 65℃, only the upper element works. It should be noted that this control approach was not based on the manufacturer's specification, as it was not provided. Fig. 4 presents the measured weather conditions from March 21st to March 23rd, 2025. In the real experiment, the daytime charging control was implemented on clear days from March 19th to May 2nd, 2025.

The water temperature setpoint was set to 57℃ during charging periods (12 PM-7 PM) and 43℃ during the discharging periods (7 PM–12 PM). On cloudy days, the ASHPWH was remotely adjusted to *Electric* mode to prevent the occurrence of the simultaneous operation of ASHPWH and RFHS.

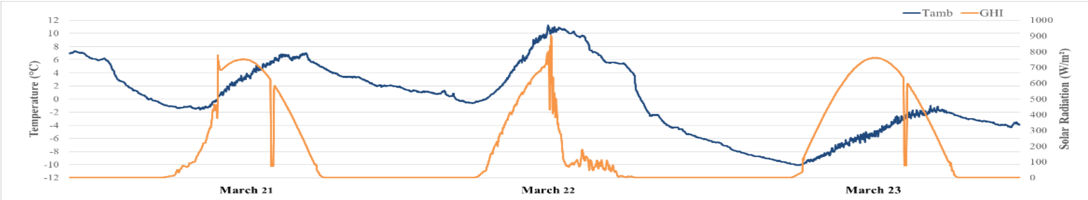

Figure 4. Outdoor air temperature and global horizontal solar radiation variations measured in Montreal from 2025/3/21 – 2025/3/23

2.5. Model predictive control (MPC)

The NMPC algorithm was developed based on the do_mpc [22] to account for the variable water mass flow rates and the system's complex nonlinear behavior. Eq.(13-21) presents the MPC algorithm, where $x^k, u^k, tvp^k,$ and s^k represent the variables of state, input, time-varying, and slack at the kth time step of the prediction horizon with a sampling time of δt. The state variables follow those of the RC thermal networks, with three additional nodes representing the water heater's top, middle, and low temperature nodes (Eq. (13)). The input variables are the heat pump on/off operation mode and the water mass flow rate for the RFHS, as shown in Eq. (14). The predicted environmental variables are ambient temperature and solar radiation (Eq. (15)). Pre-defined time-varying parameters are the Test Cell 3 measured air temperature, Test Cell 4 indoor air temperature setpoint, the electricity input for the compressor operation, the heat transfer rate of the condenser, the temperature of the air outlet of ASHPWH, the penalty for deviating from the acceptable temperature range, and the temperature of host building (Eq. (16)). The heat transfer rate of the condenser and work input, calculated based on experimental data, were used as time-varying parameters to reduce computational load. The soft constraints are applied to the state variables, as identified in Eq. (17). The prediction horizon was set to 12 hours and the control horizon to 3 hours, based on the iterative tuning. Extending the prediction horizon beyond 12 hours produced negligible performance improvements while substantially increasing computational time, largely due to the small 3-minutes simulation time step and complexity of the energy system.

The optimization function accommodates 1) minimizing the energy consumption of the ASHP, 2) maintaining optimal indoor thermal conditions, 3) encouraging binary decisions for ASHP operation, 4) regulating actuators to avoid large or sudden movement, and 5) penalizing the soft constraints, as shown in Eq. (18). It was solved using CasADi's NLPSOL interface. The same air setpoint profile from the rule-based control strategy was applied, with the minimum and maximum boundaries of 18℃ and 28℃. This boundary was applied to all indoor temperature nodes. The water temperature was constrained between 40℃ and 56℃. Overheating conditions (T_{air4} > 28°C) were assigned with the highest penalty, proportional to the magnitude of the temperature difference between setpoint and indoor air temperature, as shown in Eq. (20). It is important to note that the HP operation input variable (u_0) was defined as a continuous variable between 0 and 1, rather than as a mixed-integer variable, to avoid the complexity and computational burden associated with using a full mixed integer nonlinear MPC formulation. To encourage binary behavior, a penalty term (Eq. (21)) was introduced, which penalizes the choice of fractional values with a higher penalty, and assigns zero penalty when $u_0 = 0$ or 1. However, because Eq. (21) does not strictly enforce the binary operation, an additional post-processing step was applied: value of u_0 above 0.5 were set to 1 and values below 0.5 were set to 0, as illustrated in Fig. 5. The input variable (u_1) for the water mass flow rate was bounded between 0.00001 and 0.14 kg/s, which is the maximum flow rate of the three-speed wet-rotor circulator. The lower bound was set above zero to ensure convergence and continuous computation while keeping the MPC computationally efficient. In the simulation function, where the selected control actions were applied, any computed water mass flow rate below 0.0001 kg/s is set to zero, as this value is effectively negligible. Furthermore, all input variables were penalized to avoid having a large control input magnitude. Fig. 5 presents a detailed flow chart of the NMPC algorithm.

$$x^k = \left[T_{air4}, T_{flr4}, T_{slab4},\ T_{walls4},\ T_{w,top},\ T_{w,middle},\ T_{w,low}\right]^k \tag{13}$$

$$u^k = \left[x_{hp},\ \dot{m}_{rfhs}\right]^k \tag{14}$$

$$d^k = [d_{outdoor}, d_{solar}]^k \tag{15}$$

$$tvp^k = [T_{air3}, T_{sp,a}, W_{in}, Q_{cond}, T_{outlet}, \pi_{sp}, T_{host}]^k \tag{16}$$

$$s^k = [s_{air4}, s_{flr4}, s_{slab4}, s_{walls4}, s_{w,top}, s_{w,middle}, s_{w,low}]^k \tag{17}$$

$$J = argmin\ (\sum_{k=0}^{PH-1}[(\pi_{hp}^k * P_{hp}^k * \delta t)] + \sum_{k=0}^{PH-1}[\pi_{sp}^k(\lambda_{sp}^k * \delta t)] + \sum_{k=0}^{PH-1}[\pi_{hp}^k(\lambda_{binary}^k * \delta t)] + \sum_{k=0}^{PH-1}[(\pi_{hp}^k u_0^k + \pi_{rfhs}^k u_1^k)\delta t] + \sum_{k=0}^{PH-1}[\pi_{slack}^k(s_{up}^k + s_{low}^k)\delta t)]) \tag{18}$$

$$P_{hp} = W_{in} * x_{hp} \tag{19}$$

$$\lambda_{sp} = (T_{air4} - T_{sp})^2 \tag{20}$$

$$\lambda_{binary} = x_{hp}(1 - x_{hp}) \tag{21}$$

$$0 < u_1 < 1\ \ and\ \ 0.00001 < u_2 < 0.14,\ \ 18 < T_i < 28\quad i = 0 - 7\quad and\ \ 40 < T_i < 56\quad i = 8 - 11$$

$$\pi_{hp}^k = 6, \pi_{rfhs}^k = 1, \pi_{sp}^k = 20\ (7\ AM\ to\ 7\ PM)\ and\ 1\ (7\ PM\ to\ 7\ AM), \pi_{slack}^k = 1e^8$$

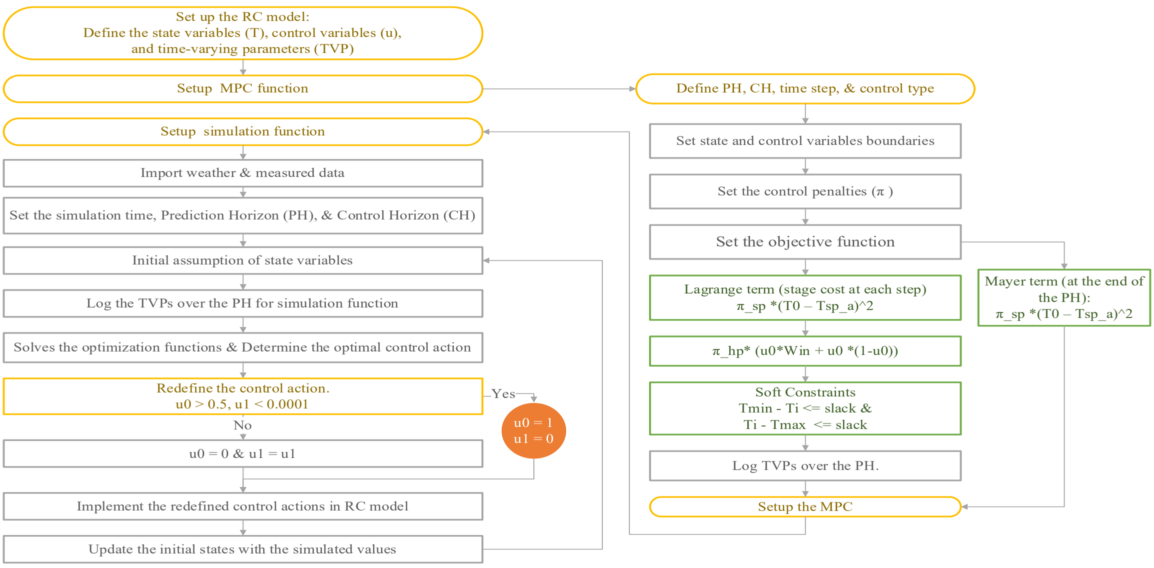

Figure 5. Flow chart of NMPC algorithm.

3. Results and Discussion

The results are presented in terms of indoor thermal conditions and energy consumption from March 22nd to 23rd. The simulated results on March 21st are excluded from the discussion, as they were influenced by the assumed initial state variables.

3.1. Case 1: Rule-based control (Reference)

Fig. 6 presents that the indoor air temperature fluctuated between 20°C and 32.5°C in the reference case, with overheating occurring for 10% of the time on March 22nd and 28.3% of the time on March 23rd. The activation of RFHS at 7 AM made the indoor air temperature rise gradually and reach the setpoint temperature around 10 – 10:30 AM. As the stored hot water was depleted in the morning with the activation of RFHS, the electric resistance elements operated between 7 AM and 12 PM to maintain the water heater setpoint of 55°C. During midday, solar gains increased indoor temperatures, allowing the building to remain warm until the next day early morning. ASHP operated intermittently when the water temperature fell slightly below 55°C, as shown in Fig. 6.B. This intermittent operation of the ASHP at night and recirculation of cooled air into Test Cell 4 produced only negligible reductions in indoor air temperature. The corresponding COP were 2.47 to

3.74, by using the Test Cell 3 air temperature ranged between 18.9°C and 29.2°C. As a result, the reference strategy made limited use of solar heat gains available in Test Cell 3 for ASHP operation during the daytime and relied primarily on the electric resistance elements to charge the water heater. Consequently, the total daily energy consumption was 1.40 kWh and 2.26 kWh on March 22nd and March 23rd, respectively.

A) B)
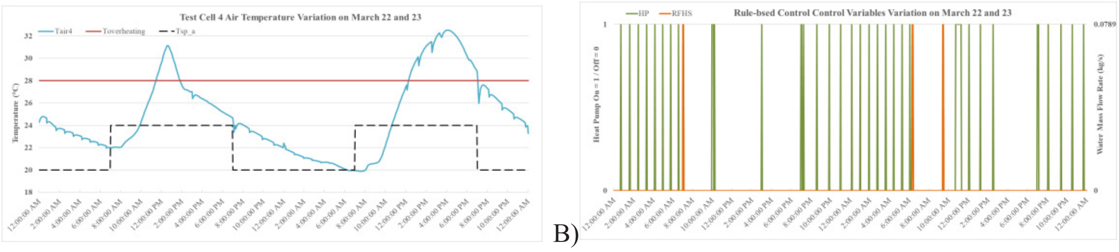

Figure 6. A) Test Cell 4 air temperature variation and B) input variables variation on March 22nd -23rd in rule-based control strategy.

3.2. Case 2: Daytime charging control

Like the reference case, the indoor air temperature varied between 20°C and 32.5°C (Fig. 7.A). On March 23rd, the RFHS was activated in the morning; however, the electric resistance elements were not used because the water setpoint was reduced to 43°C in this control approach. When the water setpoint was increased to 55°C for charging at noon, the ASHP operated for 2-3 hours using the preheated air from Test Cell 3. Simultaneously, ASHP recirculated 10-14°C outlet air and reduced the indoor air temperature to 24°C - 27°C. Once the charging period ended, the indoor air temperature rose back to around 23 - 24°C. However, on March 22nd, even before the charging period began, the air temperature increased up to 29.6°C, and then decreased to 24 - 27°C. These different temperature variations occurred because the daytime charging control used a fixed charging window and lacked the flexibility to adapt its operation according to future weather forecasts. Consequently, overheating occurred for 2.5% of the time one March 22nd and 19.4 % of the time on March 23rd – representing reductions of 75% and 31.4% compared to the reference case. Favourably, as the charging period was during the daytime, the ASHP operated more efficiently at a COP of 3.5-4.8, by using the air source at 27.4°C −36.3°C. This efficient operation and minimal operation of electric resistance reduced the total daily energy consumption to 0.40 kWh and 0.68 kWh on March 22nd and 23rd, respectively. However, despite this 70% reduction in energy use compared to rule-based control, both control strategies remained ineffective in maintaining thermally satisfying indoor conditions. This limitation arises from the lack of system communication and the inability to respond to the dynamic outdoor conditions, leading to uncoordinated and conflicting heating and cooling operations.

A) B)
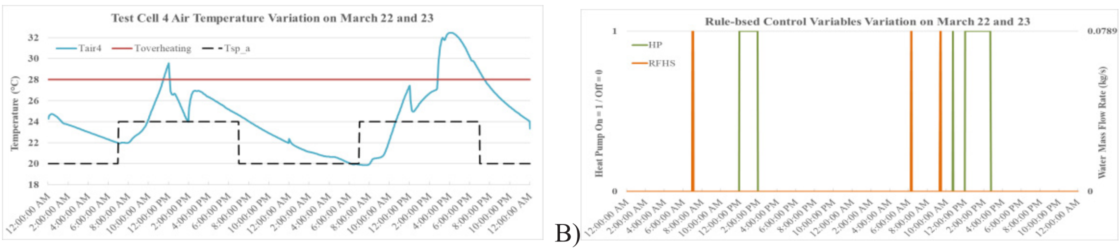

Figure 7. A) Test Cell 4 air temperature variation and B) input variables variation on March 22nd -23rd with daytime charging control strategy.

3.3. Case 3: Model predictive control

Under the MPC approach, the indoor air temperature fluctuated between 18°C and 29°C, overheating for 4.2% of March 22nd and 16.9 % of March 23rd, which is respectively 58% and 40.2% less overheating than the reference case. The MPC strategy operated the RFHS earlier than other cases, and after 7 AM, stopped the continuous operation, by anticipating substantial solar heat gains later in the day (Fig. 8). As the water temperature fell below the setpoint temperature and the indoor air temperature exceeded 28°C, the ASHP was activated intermittently to charge the water heater and simultaneously supply cooled air. The water heater did not follow a specific charging-discharging setpoint profile in MPC, but it was maintained between 40°C and 56°C the whole time. However, the NMPC could not eliminate overheating completely because its ability to recharge on the following day was constrained by the limited TES capacity and the low usage of the stored water for nighttime heating. To better understand its applicability, the performance of this solar-driven TES mechanism should be further evaluated in colder climates, where heating loads are significantly greater, or in diversified water usage conditions. In the current condition, to maintain ASHP operation even after the tank reached its setpoint temperature, the MPC intentionally discharged a small amount of stored hot water (< 0.001 kg/s) to the RFHS in the afternoon. Therefore, highly oscillating ASHP operation occurred. At night, indoor air temperatures gradually decreased to 20℃-22℃. Overall, by using the high-temperature air source and implementing effective operation of ASHPWH-RFHS, the total energy consumption was 0.17 kWh and 0.57 kWh on March 22nd and March 23rd, representing 88% and 75% reductions compared to the reference, and 58% and 15% reductions compared to the daytime charging control strategy. These results demonstrate that stored water usage control and thermal energy storage capacity have significant roles in determining the operational behavior of the ASHPWH-RFHS.

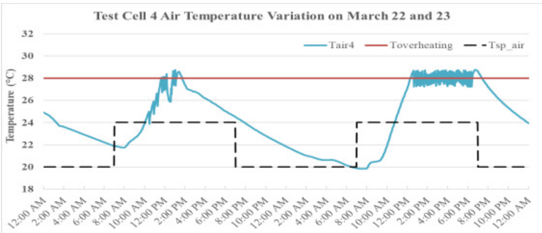

A)

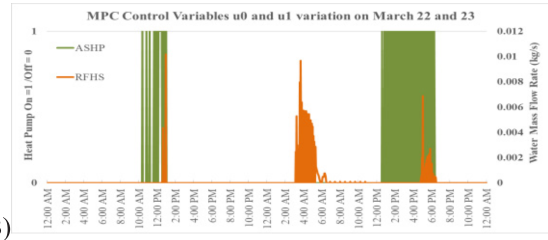

B)

Figure 8. A) Test Cell 4 air temperature variation and B) MPC input variables u_0 and u_1 variation on March 22nd -23rd with MPC.

Table 2. Total energy consumption by ASHP and % of daily overheating conditions on March 22nd and 23rd

Control Strategies	Daily energy consumption for ASHP (kWh)		% of day in overheating condition	
	3/22	3/23	3/22	3/23
Reference	1.40	2.25	10	28.3
Daytime Charging	0.40	0.68	2.5	19.4
MPC	0.17	0.57	4.2	16.9

The results indicate that even advanced control strategies are constrained in effectiveness when the physical system lacks adequate storage capacity. This underscores the need to identify critical design parameters through sensitivity analysis and to develop system design and control strategies in parallel from the early stages to ensure the optimal building energy performance. Additionally, coordinated use of active shading and ventilation could substantially improve system performance and prevent overheating by reducing reliance on the heat pump as the sole cooling mechanism. Shading systems can instantaneously reduce solar heat gain, while ventilation systems can introduce fresh outdoor air to support cooling. Therefore, future work should focus on developing an integrated optimization framework that coordinates various active energy systems to avoid unnecessary auxiliary operations and enhance overall system efficiency. Looking ahead, a BIPV/T system will be installed on the roof of the FBL to convert solar energy into both electrical and thermal energy. The preheated air from BIPV/T could serve as the air source for the ASHP, diversifying the air source and enabling more effective heat transfer in the ASHPWH.

4. Conclusions

This research proposes an NMPC framework to optimize the operation of an integrated ASHPWH-RHFS system that utilizes preheated air from a solarium and recirculates the exhausted air from ASHP for cooling. A low-order RC thermal network model and a discretized water heater model were developed to represent the indoor thermal dynamics and to compute the total energy consumption of the ASHPWH. The daytime charging control strategy was conducted in FBL in Montreal, Canada, from March to May 2025. The calibrated RC model was used to evaluate the system performance under three control strategies: rule-based control, daytime charging control strategy, and NMPC. The NMPC algorithm was formulated to control the on/off operation of ASHP and the water mass flow rate of RFHS with the goal of minimizing energy consumption and maintaining thermally comfortable conditions. Results present that NMPC maintained the indoor thermal conditions within the comfort range for 83.1% of the day on March 23rd, while limiting the peak indoor air temperature to 29℃.

In contrast, the reference and daytime charging control strategies maintained acceptable indoor conditions for 71.7% and 80.6% of the day on March 23rd, respectively, while peak temperature reaching 32.5℃. Moreover, the NMPC reduced daily energy consumption by 88% compared to the reference case, by improving ASHP's COP by 58% through effective use of warm air from the solarium. However, the limited thermal energy storage capacity and the relatively low water usage constrained the controller's ability to initiate consistent charging cycles. To better understand its potential, future research should evaluate its performance under colder conditions, where substantially higher heating loads are required, or diversify the water end-usage. Moreover, the results emphasize the need to concurrently develop system design and control strategy to maximize overall building energy performance. Future studies should focus on identifying the key design parameters of the ASHPWH-RFHS system and optimizing the system design by using a predictive control-based approach. Additionally, the operation of the integrated active energy system, including active shading, lighting, and ventilation, should be further investigated to improve overall building energy performance. In conclusion, this research demonstrates the effectiveness of NMPC in enhancing the energy efficiency of an integrated energy system and maintaining more favorable indoor conditions in a solar house compared to both the reference and daytime charging control methods.

5. Nomenclature

α = Absorption coefficient of the pipelines (-)
C = Thermal capacitance (J/°C)
c_p = Specific heat at constant pressure (J/kg/°C)
$\dot{m}$= Mass flow rate (kg/s)
p = Time interval (s)
Q = Heat transfer rate (W)
R = Thermal resistance (m^2°C/W)
T = Temperature (°C)
t = Time (s)
tvp = Time varying parameters
$\Delta t_{critical}$ = Critical time step (s)
U = Thermal conductance (W/ m^2°C)
u = Input variables
W_{in} = Work input to compressor (W)
x = Binary input variables (-)
π = Penalty (-)

6. Subscripts

a = air
air3/ air4 = air node in Tet Cell 3 or 4
cond = condenser
conv = convection heat transfer in water
cooling = cooling heat transfer rate
elec = electric resistance element
evap = evaporator
outlet = evaporator outlet air
flr4 = floor node in Test Cell 4
host = host building
i = current node
j = adjacent node
low = low control volume of a water heater
middle = middle control volume of water heater
n = temperature node
P = power
pipe = RFHS pipe system
outdoor = outdoor air
return = return water from RFHS
slab = inside of the concrete slab
solar = solar radiation
solargain = solar heat gain
sp = setpoint temperature profile
top = top control volume of water heater
w = water
walls4 = walls and ceiling node in Test Cell 4

7. Acronyms

ASHPWH = Air-source heat pump water heater
COP = Coefficient of performance
CV(RMSE) = Coefficient of variation of root mean squared error
FBL = Future Buildings Laboratory
MPC = Model predictive control
NMBE = Normalized mean bias error
NMPC = Nonlinear model predictive control
RC = Resistance-Capacitance
RFHS = Radiant floor heating system

Acknowledgements

The authors acknowledge the financial support of the National Sciences and Engineering Research Council of Canada (NSERC) through the NSERC/Hydro-Québec Alliance Research Chair and Canada First Research Excellence Fund through the Volt-Age. Yearim Yang also acknowledges the Fonds de recherche Québec for the doctoral research scholarship support and Dr. Jiwu Rao and Jing Li for their support in conducting the experimental work.

References

[1] International Energy Agency. Global Energy Review 2025 [Internet]. Paris; 2025 Mar [cited 2026 Jan 6]. Report. Available from: https://www.iea.org/reports/global-energy-review-2025

[2] Péan T. Heat Pump Controls to Exploit the Energy Flexibility of Building Thermal Loads [Internet]. Universitat Politècnica de Catalunya— BarcelonaTech; 2021. Available from: http://www.springer.com/series/8790

[3] Sun W, Wei X, Zhou B, Lu C, Guo W. Greenhouse heating by energy transfer between greenhouses: System design and implementation. Appl Energy. 2022 Nov 1;325. doi:10.1016/j.apenergy.2022.119815

[4] Moran MJ, Shapiro HN, Boettner DD, Bailey MB. Fundamentals of Engineering Thermodynamics 9th Edition. 9th ed. Ratts L, editor. Don Fowley; 2018. 370–373 p.

[5] Zhai P, Li J, Lei T, Li R, Novakovic V. Application of heat pump assisted solar evacuated tube water heater operated within passive solar house in severe cold region. Renew Energy. 2024 Dec 1;237. doi:10.1016/j.renene.2024.121629

[6] Ma Q, Chen X, Wang X, Gao W, Wei X, Fukuda H. A review of the application of sunspace in buildings. Energy Sources, Part A: Recovery, Utilization and Environmental Effects. Taylor and Francis Ltd.; 2025. p. 10292–314. doi:10.1080/15567036.2021.1963884

[7] Touchie MF, Pressnail KD. Evaluating a proposed retrofit measure for a multi-unit residential building which uses an air-source heat pump operating in an enclosed balcony space. Energy Build. 2014;85:107–14. doi:10.1016/j.enbuild.2014.08.048

[8] Gaucher-Loksts E, Athienitis A, Ouf M. Design and energy flexibility analysis for building integrated photovoltaics-heat pump combinations in a house. Renew Energy. 2022 Aug 1;195:872–84. doi:10.1016/j.renene.2022.06.028

[9] Park B, Rempel AR, Mishra S. Performance, robustness, and portability of imitation-assisted reinforcement learning policies for shading and natural ventilation control. Appl Energy. 2023 Oct 1;347. doi:10.1016/j.apenergy.2023.121364

[10] Fernandez N, Xie Y, Katipamula S, Zhao M, Wang W, Corbin C. Impacts of Commercial Building Controls on Energy Savings and Peak Load Reduction. 2017. Report.

[11] Liu D, Zhao J, Tian Z, Li Y, Yang Z, Lu S, et al. Optimization of hybrid active-passive solar heating system through day-ahead and real-time control. Energy. 2025 May 15;323. doi:10.1016/j.energy.2025.135816

[12] Reynders G, Nuytten T, Saelens D. Potential of structural thermal mass for demand-side management in dwellings. Build Environ. 2013 Jun;64:187–99. doi:10.1016/j.buildenv.2013.03.010

[13] Rastegarpour S, Gros S, Ferrarini L. MPC approaches for modulating air-to-water heat pumps in radiant-floor buildings. Control Eng Pract. 2020 Feb 1;95. doi:10.1016/j.conengprac.2019.104209

[14] Hill J. Methodology for the Design and Predictive Control of Active Solar Windows with Radiant Floor Heating in Perimeter Zones. [Montreal]: Concordia University; 2023.

[15] Rheem Canada Ltd. SSEC CPROPH50T RH375-30. 2020 Jun.

[16] Jutras N. Energy Star. 2024. What is Uniform Energy Factor and Why Does it Matter?

[17] Energy350. Heat Pump Water Heater Performance Results. 2018.

[18] Athienitis A. Buiding Thermal Analysis. MathSoft,Inc.; 1998.

[19] Newville M, Stensitzki T, Otten R. Non-Linear Least-Squares Minimization and Curve-Fitting for Python. 2025.

[20] Muehleisen RT, Bergerson J. Purdue e-Pubs Bayesian Calibration-What, Why And How Bayesian Calibration-What, Why And How [Internet]. Report. Available from: http://docs.lib.purdue.edu/ihpbc

[21] American Society of Heating Refrigerating and Air-Conditioning Engineers Inc. ASHRAE Guideline 14 Measurement of Energy and Demand Savings. Atlanta; 2002.

[22] Fiedler F, Karg B, Lüken L, Brandner D, Heinlein M, Brabender F, et al. do-mpc: Towards FAIR nonlinear and robust model predictive control. Control Engineering Practice. 2023.